Remote Sensing of Environment 164 (2015) 103–113

Contents lists available at ScienceDirect

Remote Sensing of Environment

journal homepage: www.elsevier.com/locate/rse

An integrated method to improve the GOES Imager visible radiometric calibration accuracy

Fangfang Yu [a,*], Xiangqian Wu [b,1]

[a] Earth Resources Technology, Inc., Laurel, MD, USA
[b] NOAA/NESDIS/STAR, College Park, MD, USA

ARTICLE INFO

Article history:
Received 20 July 2014
Received in revised form 6 March 2015
Accepted 1 April 2015
Available online xxxx

Keywords:
GOES Imager visible channel
GOES-R ABI
Vicarious calibration
DCC
Desert
Ray-matching
Integrated calibration
Recursive filtering
Calibration accuracy

ABSTRACT

A variety of vicarious calibration methods over different reference targets have been studied at National Oceanic and Atmospheric Admission (NOAA)/National Environmental Satellite, Data, and Information Service (NESDIS) to provide sensor degradation information for the GOES Imager visible channels which do not have any on-board calibration devices. To meet the increasing demand for more accurate satellite measurements, an integrated method is developed mainly to improve the relative calibration accuracy by combining the results from different vicarious methods. In this study, three commonly used vicarious calibration methods, the desert, Deep Convective Cloud (DCC) and ray-matching methods, are applied to the GOES-12 Imager visible data to describe the integrated method. The integrated method first combines the normalized observations of each individual method by anchoring the results on the first day of satellite operation, and then removes the deviated combined observations using a recursive filtering method. This integration is based on the fact that the GOES sensor trending functions from different methods are very similar within 1% difference over the 7-year study period. The trending uncertainty of the integrated method is less than that of each individual one. The absolute calibration of the integrated method can be achieved by generating the calibration coefficients using the reflectance of reference targets which are well characterized with the Aqua MODIS Collection 6 (C6) data. It is found that there is less than 1% difference between the calibration coefficients derived with the DCC and desert reference targets. It is expected that this integrated method will be a useful tool to validate the GOES-R ABI on-board radiometric calibration accuracy for the solar reflective channels.

© 2015 Elsevier Inc. All rights reserved.

1. Introduction

The Geostationary Operational Environmental Satellites (GOES) are a series of geostationary (GEO) satellites operated by the National Oceanic and Atmospheric Administration (NOAA)/National Environmental Satellite, Data and Information Service (NESDIS) for weather nowcasting and meteorology and climate researches of the Western Hemisphere. The GOES Imager is a multiple channel imaging radiometer designed to sense radiant and solar-reflected energy from the environs of the United States and its neighbors. Each Imager instrument has one visible and four infrared channels. The solar-reflected channel provides high spatial resolution daytime cloud imageries which are critical for the land and sea surface temperature products (Hayden, Wade, & Schmit, 1996; Maturi et al., 2008; Wu, Menzel, & Wade, 1999). They are also widely used in the generations of many other GOES Imager geophysical products such as snow mapping (Romanov, Gutman, & Csiszar, 2000), GOES aerosol and smoke (Knapp, 2002), wildfire burning biomass and biomass burning emissions (Prins, 1996; Zhang, Kondragunta, Ram, Schmidt, & Huang, 2012), icing enhanced cloud top altitude (Ellord & Bailey, 2007), cloud properties (Chepfer, Minnis, Young, Nguyen, & Arduini, 2002), and top-of-atmosphere radiation budget (Pinker et al., 2003).

High quality of calibrated satellite radiance is fundamental to accurate retrieval of the geophysical products. Unfortunately, designed for weather imaging applications, no on-board calibration device is available for the current GOES visible channels. Vicarious calibration, which uses not-in-orbit stable object as the calibration reference target, is employed to examine the sensor in-orbit degradation patterns or provide the post-launch calibration coefficients. The calibration reference targets include invariant sites on the Earth such as deserts and snow/ice sites (Cosnefroy, Leroy, & Briottet, 1996; Six, Fily, Alvain, Henry, & Benoist, 2004), deep conductive cloud (DCC) (Doelling, Nguyen, & Minnis, 2004a), and Rayleigh scattering and sun-glint over clear ocean surface (Fougnie, Henry, Morel, Antoine, & Montagner, 2002; Hagolle, Nicolas, Fougnie, Cabot, & Henry, 2002), collocated measurements with well-calibrated Low-Earth-Orbit (LEO) instruments (Doelling, Minnis, & Nguyen, 2004b), and extraterrestrial targets (Bremer, Baucom, Vu, Weinreb, & Pinkine, 1998; Kieffer & Stone, 2005). It assumes that the time-series of the observations of the stable reference targets, either the direct satellite measurements or the ratios of satellite measurements to modeled simulations of the reference, should be

* Corresponding author. Tel.: + 1 301 683 3553.
E-mail addresses: Fangfang.Yu@noaa.gov (F. Yu), Xiangqian.Wu@noaa.gov (X. Wu).
[1] Tel.: +1 301 683 3603.

http://dx.doi.org/10.1016/j.rse.2015.04.003
0034-4257/© 2015 Elsevier Inc. All rights reserved.

scattered along a trending that can be used to describe the instrument degradation pattern. The performance of the reference targets should be well understood and characterized to estimate and understand the calibration uncertainty. The short-term variations of the reference targets, when well understood and characterized, can be removed or simulated to improve the calibration accuracy (Wu, Stone, Yu, & Han, 2006). To reduce the risk of erroneous degradation trending, multiple calibration methods are often used to cross-check the results. In fact, a variety of vicarious calibration methods using different stable targets have been studied for the GOES Imager visible channels, including the Sonoran desert (Rao, 2001; Yu, Wu, Grotenhuis, & Qian, 2014), DCC (Yu & Wu, 2013), the Moon (Wu et al., 2006), stars (Bremer et al., 1998; Chang et al., 2012), and cloud pixels collocated with MODIS Resolution Imaging Spectroradiometer (MODIS) (Wu & Sun, 2005).

The vicarious methods based on these reference targets can provide either relative or absolute calibration correction coefficients. The Sonoran desert, one of the largest deserts in North America which can be observed by both GOES-East and GOES-West satellites is long-term stable and thus can be used to serve as a reference target for the development of long-term GOES visible climate data with calibration accuracy traceable to Aqua Moderate Resolution Imaging Spectroradiometer (MODIS) Collection 6 (C6) data at about 3–4% (Yu et al., 2014). However, due to the impacts of strong bidirectional reflectance distribution function (BRDF) effect and occasional climate variations such as El Nino Southern Oscillation (ENSO) events, it is not an appropriate reference target for operational or near real-time data calibration. The DCC, with its high reflectance and relatively flat spectra in the visible wavelength, can be used as a stable reference target to provide absolute calibration accuracy of less than 3% for the GEO visible channels (Doelling, Morstd, Bhatt, & Scarino, 2011). Available to all the earth observation satellites, DCC is selected by the Global Satellite Inter-Calibration System (GSICS) community, an international collaboration to enhance calibration and validation of satellite observations, as a common reference to inter-calibrate the visible channels at different satellite instruments. The United States Geological Survey (USGS) lunar irradiance model based on the Robotic Lunar Observatory (ROLO) measurements can provide the time-series of lunar irradiance with high relative calibration accuracy (<1%) at certain moon phase angle ranges (Kieffer & Stone, 2005). However, there is relatively large uncertainty in the absolute calibration accuracy. Using the USGS modeled irradiance as the reference, the uncertainty of the GOES visible sensor degradation trending is about 2–3% (Wu et al., 2006), most likely due to the uncertainties in the modeled irradiance at different lunar phase angles and the GOES lunar irradiance measurements (Eplee et al., 2011; Lacherade, 2013; Yu, Wu, Stone, & Sindic-Ranic, 2013). Recent development of star radiometric calibration shows that star observations, which are originally used for the GOES navigation calibration, can provide uncertainty of sensor degradation trending comparable to the other vicarious methods (Bremer et al., 1998; Chang et al., 2012). No absolute calibration data is currently available for the star observations yet. The collocated GEO–LEO scenes identified with the ray-matching method can provide direct inter-comparison between GOES and well-calibrated LEO instrument like MODIS and Visible Infrared Imaging Radiometer Suite (VIIRS). However, the lack of coincident hyperspectral measurements to correct the spectral response difference between the GEO and LEO instruments can result in large calibration uncertainty (Wu, Qian, & Yu, 2011). To reduce the uncertainty caused by the different spectra over the same collocated scenes, current GOES Imager visible operational calibration algorithm used the GOES and Terra MODIS collocated cloud pixels which have relatively flat spectra to generate the operational calibration coefficients (Wu & Sun, 2005). The calibration uncertainty of this method is about 3% traceable to the reference standard of Terra MODIS (Yu et al., 2014). The Rayleigh and sun-glint methods have been used to provide absolute radiometric calibration accuracy at 2–4% for the LEO solar reflective channels (Fougnie et al., 2002; Hagolle et al., 2002). Yet the lack of near-infrared channels at GOES Imager prevents the direct applications of these two absolute calibration methods to the GOES visible data.

With recent development of numerical weather prediction models and global climate studies, there is an increasing demand from the user community for more accurate satellite measurements. The main objective of this study is to develop an integrated method that is capable of combining multiple vicarious calibration methods, either relative or absolute ones, to improve the radiometric calibration accuracy of the solar reflective channels. Three vicarious calibration methods (desert, DCC, and ray-matching methods) are applied to GOES-12 (located at 75°W above the Equator) to describe this method. These three methods are selected because they are applicable to most GEO solar reflective channels. As recommended by the GSICS community, Aqua MODIS C6 data is used as the community best-practice standard for the inter-calibration of solar reflective channels. Thus, the absolute calibration is achieved by providing post-launch calibration coefficients traceable to the Aqua MODIS C6 Band 1 (0.65 μm) standard. The 1 km spatial resolution of GOES and Aqua MODIS C6 data are used for this study. The MODIS data were downloaded from MODIS Level 1 and Atmosphere Archive and Distribution System (LAADS Web) at http://ladsweb.nascom.nasa.gov, while the GOES Imager data were downloaded from NOAA's Comprehensive Large Array-data Stewardship (CLASS) at http://www.class.ncdc.noaa.gov.

2. DCC, desert and ray-matching vicarious calibration methods

Fig. 1 shows the GOES and MODIS spectral response functions (SRF), as well as the spectra of DCC, high-reflectance cloud, and the Sonoran desert measured with different hyperspectral radiometers and the atmospheric transmission simulated with Line-by-Line Radiative Transfer Model (Clough et al., 2005). The GOES SRF is much wider than that of MODIS Band 1, covering some strong atmospheric absorptive lines and the rapid change of surface vegetation spectra near the near-infrared wavelength. Therefore the sensitivity of GOES visible channel top-of-atmosphere (TOA) reflectance to the variations of atmospheric absorption, molecular scattering, and, vegetation coverage can be quite different from that of MODIS Band 1. The reflectance is very different at the different reference targets within the GOES spectral range: 20–35% at the Sonoran Desert, more than 50% for cloudy pixels as selected in this paper, and over 90% for DCC pixels. Although the spectra of all the three reference targets show some variations at the strong atmospheric absorption lines, the reflectance of the Sonoran desert in general progressively increases with wavelength and the two cloud references are relatively flat.

2.1. Sonoran Desert based calibration

Recent study shows that the Sonoran Desert ([32.05°–32.35°N, 114.4°–114.7°W]) is long-term spectrally, radiometrically and spatially stable at GOES viewing geometries (Yu et al., 2014). It can be used as pseudo-invariant calibration site to develop the long-term climate data. To minimize the calibration uncertainties caused by large solar zenith angles, the GOES-12 visible data over the Sonoran desert are archived everyday around the local noontime (~19:19Z, local time at 12:19 pm) during its operational mission period from April 1, 2003 to April 14, 2010.

According to Yu et al. (2014), the time-series of the pre-launch calibrated clear-sky desert reflectance can be described with a quadratic function to simulate the instrument degradation and two terms of sine functions to describe the combined effects of desert BRDF, atmospheric component variations and possible surface changes which have seasonal variations (Eq. 1). In this study, monthly mean clear sky desert reflectance are used for the trending analysis, in consistent with the time intervals used in the other two methods, the DCC and ray-matching methods (Doelling et al., 2004a; Wu & Sun, 2005). Fig. 2 displays the results of the procedures to generate the desert-based

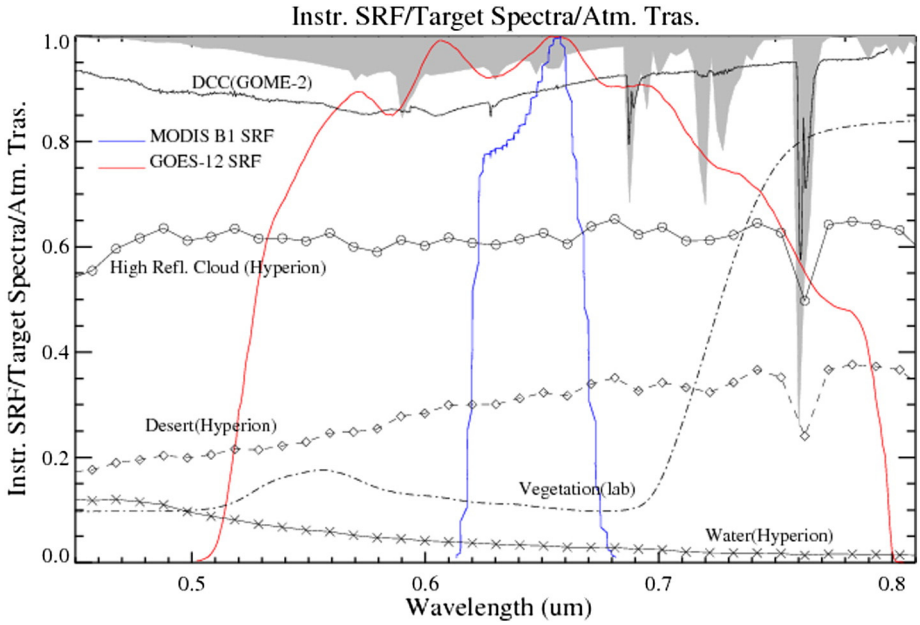

Fig. 1. SRFs of GOES-12 Imager visible channel and Aqua MODIS Band 1, as well as the spectra of DCC (measured with Metop-A/GOME-2 Bands 3 and 4, from 0.392 to 0.798 μm), Sonoran Desert (Hyperion measurements), and cloudy pixels (mean Hyperion measurements from a cloud image obtained over a Hurricane event). Plotted also include the clear water (Hyperion measurements) and vegetation (USGS Spectroscopy Lab measurements, http://speclab.cr.usgs.gov) spectra, and the atmospheric transmissions simulated with Line-by-Line Radiative Transfer Model using clear tropical ocean atmospheric profile (Clough et al., 2005) (in gray shadow).

monthly observations. The daily median TOA reflectance of the desert pixels within the study area is shown in Fig. 2a. Fig. 2b shows the daily median TOA reflectance after removing of cloud-contaminated pixels and the consequently generated monthly mean reflectance. The algorithms to screen the cloud contaminated pixel reflectance are described in Yu et al. (2014), using the combination of threshold and recursive filtering methods. The monthly clear-sky desert reflectance in Fig. 2b is fitted with Eq. (1). The monthly desert reflectance after the removal of seasonal variations shown in Fig. 2c is the combination of sensor degradation and the residual of the seasonal fittings and will be used for the further analysis in this study. Anomalous low reflectance can be observed in Fig. 2c in the year of 2005, coincident with the strong ENSO event in 2005 (Wu, personal communication). Similar large reflectance deviation in 2005 was also reported in the time-series of MODIS data at the same area and was believed relative to the abnormally large rainfall in early 2005 (Angal, Chander, Xiong, Choi, & Wu, 2011). Deviations due to the short-term correction residuals with the sine functions can be also observed in Fig. 2c.

$$R_{pre,t} = a + bt + ct^2 + m_1 \sin(\alpha t + \beta_1) + m_2 \sin(2\alpha t + \beta_2) \quad (1)$$

where $R_{pre,\,t}$ is the clear-sky desert reflectance at time t calculated with pre-launch calibration coefficients; the first term, $a + bt + ct^2$, is used to account for the sensor degradation, while the two sine terms are for the corrections of seasonal variations; α is the frequency of the annual variation calculated as $2\pi/days_in_a_year(days_in_a_year = 365.25)$; and β_1 and β_2 are the phase angles. The parameters of a, b, c, m_1, m_2, β_1 and β_2 are estimated using least-squares fitting, and t is the time (in day or year) since the satellite became operational. The pre-launch calibration coefficients can be found at GOES Variable Format (GVAR) and are also available at the webpage: http://www.star.nesdis.noaa.gov/smcd/spb/fwu/homepage/GOES_Imager_Vis_PreCal.php.

2.2. Ray-matching method

Ray-matching method is a direct sensor-to-sensor inter-comparison between GEO and LEO. It uses coincident, co-angled and geographically collocated pixels to transfer the GEO measurements to the well-calibrated LEO measurements (Doelling et al., 2004b). The collocations with similar viewing and solar illumination geometries within a short time interval can greatly reduce the impacts of dynamic atmosphere between the surface and the satellites. In this study, the GOES and Aqua/MODIS data collocations are obtained using the following criteria, similar to those applied in the current operational method between GOES and Terra/MODIS (Wu & Sun, 2005): 1) the central locations of the collocated MODIS and GOES pixels should be less than 1 km; 2) the GEO and LEO over-passing time difference is less than 10 min; 3) to minimize the BRDF impact caused by large viewing zenith angles, the collocated pixels should occur within $\pm 10°$ latitude and longitude from the GOES sub-satellite region; and 4) the viewing zenith angle (θ) difference, calculated as $\left|\frac{\cos(\theta_{leo})}{\cos(\theta_{geo})} - 1\right|$, is less than 1% to minimize the impact of different optical paths through the atmosphere. No azimuthal angle match criteria are applied to select the pairs. The GEO–LEO collocations of GOES-12 occur at every two to five days at the ascending Aqua orbits.

As shown in Fig. 1, the different GOES and MODIS SRFs can result in different reflectance values over the collocated scenes, specially for the vegetation scenes of which the GOES reflectance can be significantly different from MODIS. The Spectral Band Adjustment Factor (SBAF) which is used to account for the SRF induced observation difference is needed for the accurate inter-calibration between GOES and MODIS (Doelling, Lukashin, Minnis, Scarino, & Morstad, 2012; Teillet et al., 2001). Due to the lack of co-incident hyper-spectral measurement of each paired pixel, it is challenging to derive the accurate scene-dependent SBAF value for the absolute calibration of GOES measurements using the ray-matching method. However, as shown in Fig. 1, the high reflectance cloud has relatively little spectra variation, suggesting that the impact of SRF difference on the observations can be greatly reduced at these cloud pairs. The direct reflectance ratio of the cloud pairs can be used for the relative calibration of the GOES Imager visible channel. In this study, the collocations with MODIS reflectance larger than 50% are identified as cloud pixels and used to reduce the SRF-induced reflectance difference. To reduce the possible mis-matches caused by the moving of the

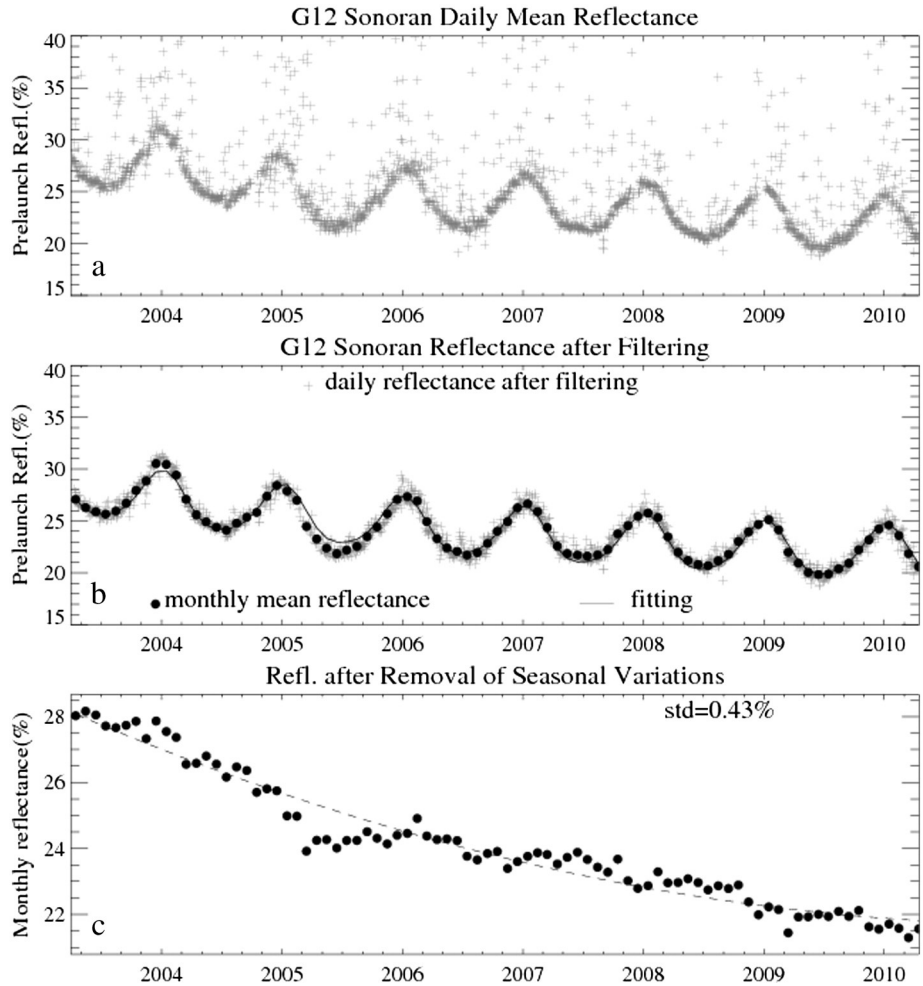

Fig. 2. Time-series of the daily median reflectance of the Sonoran desert (a); time-series of daily median reflectance after contaminated pixel filtering (in gray plus), monthly mean of the daily clear-sky reflectance (in solid dots), and fitting of the monthly mean reflectance (black line) (b), and time-series of reflectance after removal of seasonal variations (c). *std* stands for the standard deviation of the fitting residuals of the time-series data.

clouds and the different navigation systems used in the two satellites, two more criteria are also applied to ensure that the two instruments view the same targets at the collocated pixels: 1) the coefficient of variation values, calculated as the standard deviation of reflectance from the 3×3 window arrays centered at the collocated pixels divided by their mean value should be less than 3% for both GOES and MODIS data; and 2) the reflectance of GOES collocated pixels should be greater than 25% (Wu & Sun, 2005). The two criteria are used to ensure that even if the GOES and MOIS are not looking at the same real cloud, but the cloud they are looking should have the same properties. In addition, the threshold of relative azimuth angle (RAA) ($30° < RAA < 150°$) is also applied to avoid the impact of the sun-glint effect.

Fig. 3 illuminates the sensitivity of the GEO–LEO collocated cloud reflectance ratio to the number of collocations using the data obtained in June 2003 which has about 20,000 cloud pairs. The Monte-Carlo method is used to calculate the reflectance ratio values for a set of cloud pair numbers ranging from 500 to almost 18,000 pairs with an interval of 100. The standard deviation of the reflectance ratios is also calculated at each given number of cloud pairs. As shown in Fig. 3, the standard deviation of the reflectance ratio decreases with the increasing number of collocated cloud pixels. In this study, the number of 5000 collocated cloud pixels which corresponds to about 0.05 standard deviation value is somehow randomly selected as the threshold to derive the reliable monthly reflectance ratio. Since the number of monthly cloud collocation pixels ranges from 7000 to 220,000 for all the months between April 2003 and April 2010, the ray-matching method derived reflectance ratio is available for each month within the study period.

Fig. 4 shows the time-series of monthly GOES and MODIS cloud reflectance ratios (primary y-axis) and the number of cloud collocations (second y-axis). The time-series of reflectance ratio can be fitted with a quadratic function to simulate the GOES degradation. There are

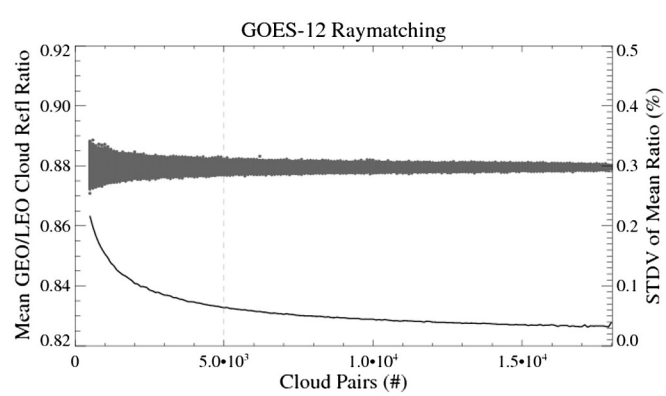

Fig. 3. Sensitivity of GOES to MODIS reflectance ratio to the number of collocated cloud pixels. The number of reflectance ratios scattered decreases with the increasing number of cloud pairs. The distribution of the reflectance ratio is plotted with the primary y-axis, while the standard deviation of the ratios (black line) for a given collocated pixel number is plotted with the second y-axis.

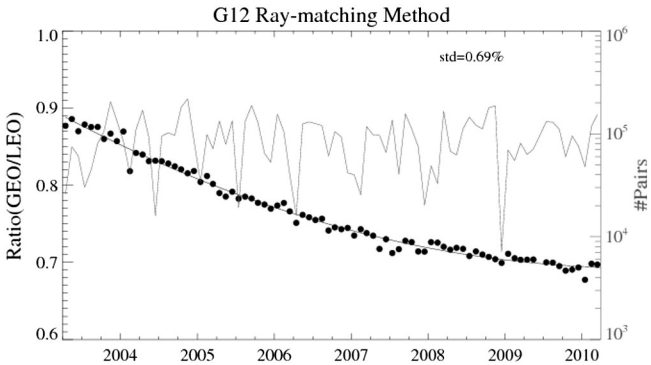

Fig. 4. Time-series of the monthly reflectance ratio between GOES and MODIS over the collocated cloud pixels (black dots with primary y-axis) and number of collocated cloud pairs (gray line with second y-axis).

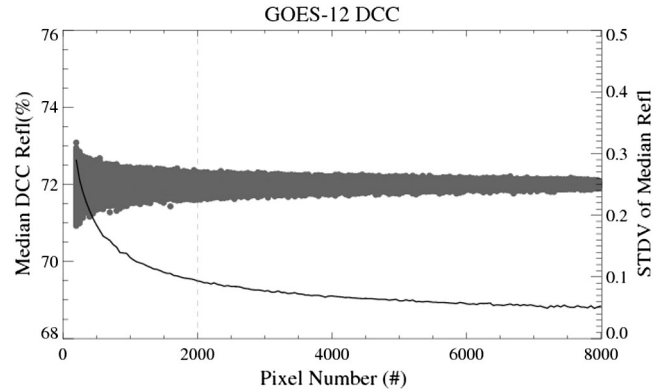

Fig. 5. Sensitivity of DCC reflectance to the randomly selected GOES-12 DCC pixels ranging from 50 to 8000. The standard deviation of the DCC reflectance (black line) is plotted with the second y-axis.

several reasons that may cause the variations in the reflectance ratio. First, although the cloud pixels have high reflectance, it is possible that some of the pixels may be partially contaminated with the spectra beneath the cloud. The strong water vapor absorption in the lower troposphere and surface vegetation reflectance, if collocated over the land, can affect the GOES cloud reflectance. Secondly, the maximum time difference between the GOES and MODIS observation is 10 min. It is thus possible that the cloud in some of the pairs may be different due to the movement of the cloud masses during the time interval. Both of these effects can affect the reflectance ratios, especially for the months with relatively few collocation numbers.

2.3. DCC method

The high reflectance of DCC is reported to be very stable with slight seasonal and spatial variations over the global sub-tropical regions (Doelling, Morstad, Scarino, Bhatt, & Gopalan, 2013). According to Doelling et al. (2004a), the criteria for DCC pixel identification include: 1) the DCC pixels should occur within the spatial region of ±20° latitude and longitude from the GOES sub-satellite point; 2) brightness temperature (Tb) of Channel 10.7 μm should be less than 205 K; 3) the Tb standard deviation for the array of 3 × 3 pixel window centered at the DCC pixel should be less than 1 K; 4) coefficient of variance of visible reflectance for the 3 × 3 pixel window is less than 3%; and 5) solar and viewing zenith angles should be less than 40°. Each DCC reflectance is corrected with the Hu et al. (2004) model for the BRDF correction.

The DCC calibration is a statistical method that relies on large amount of identified DCC pixels. The DCC reflectance is typically represented with the mode value from the histogram of monthly DCC reflectance (Doelling et al., 2004a). For GOES-12, the variation of median DCC reflectance is slighter smaller than that of mode value derived from DCC reflectance probability distribution function (Yu & Wu, 2014). The median reflectance value of the monthly DCC pixels is thus used to describe the monthly DCC reflectance. As the robust DCC reflectance depends on sufficient DCC pixels, a sensitivity study with GOES-12 DCC pixels obtained in July 2005 is used to calculate the DCC reflectance from a large range of number of randomly selected DCC pixels. As shown in Fig. 5, the variations of median DCC reflectance decrease as the number of DCC pixels increases. In this study, a minimum of 2000 DCC pixels is randomly used as the threshold for a reliable monthly DCC reflectance. The time-series of GOES-12 DCC monthly median reflectance is shown in Fig. 6. The slightly seasonal variation of the time-series DCC reflectance is probably attributed to the variation of the cloud microphysics as the DCC spatial locations change seasonally (Doelling et al., 2013).

The reflectance of DCC reference target is calculated with the time-series of MODIS DCC reflectance derived from the ray-matching method (Fig. 7). The minimum of 2000 DCC pixel number is also applied for a reliable monthly MODIS DCC reflectance. An anomaly of low DCC reflectance was observed in March 2008. An examination of the MODIS DCC pixels in this month showed that the DCC pixels in this month were dominated with the data obtained on 29 March 2008 which had very low reflectance (60–70%) at Tb range of 204–205 K. The relatively high Tb values and low reflectance suggested that these identified pixels were unlikely real DCC pixels. Future research is needed to understand the physics of DCC cloud particles for the better understanding of DCC performance. No significant trending can be observed from the time-series of monthly MODIS DCC reflectance. When the outlier of March 2008 data is excluded, the mean of the monthly median DCC reflectance is 88.87% (±1.92%), which will be used for the absolute calibration later in this paper.

3. Integration of multiple vicarious calibration methods

3.1. Combination of vicarious calibration results

Three steps are applied to combine the results from different calibration methods. First, a quadratic function is used to fit the time-series observations of each vicarious calibration (Eq. 2). For the desert method, the time-series of observations are the monthly pre-launch calibrated reflectance after the removal of seasonal variations as shown in Fig. 2c. The observations of the DCC method are the monthly pre-launch calibrated DCC reflectance (Fig. 6), and the observations of the ray-matching method are referred to the monthly mean ratios between the GOES and MODIS collocated cloud reflectance (Fig. 4).

$$S_{t,i} = a_i + b_i t + c_i t^2 \tag{2}$$

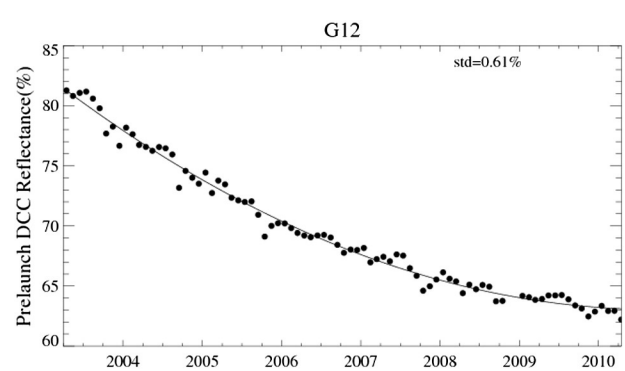

Fig. 6. The time-series of GOES-12 DCC reflectance represented as the median values.

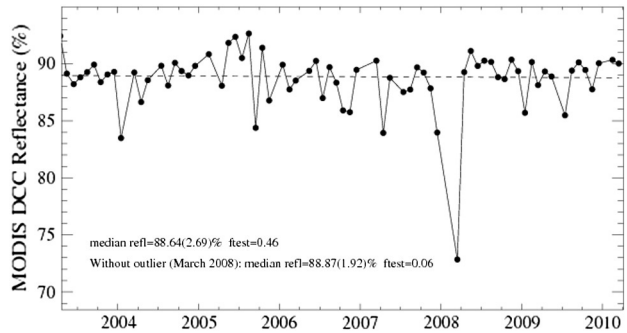

Fig. 7. Time-series of Aqua MODIS C6 DCC reflectance represented with median values. The DCC reference reflectance is generated from the MODIS ray-matching DCC pixels. The result of the ftest shows no significant trending in the time-series of MODIS monthly DCC reflectance, with or without the outlier in March 2008. The dash line is the mean of the monthly median reflectance without the outlier (88.87%).

Where $S_{t,i}$ are the monthly observation of method i at time t; t is the time (in day or year) after the satellite became operation; and a_i, b_i, and c_i are the quadratic fitting coefficients.

The second step is to normalize the monthly observations of each method to the value estimated on the first day of satellite operation (Day 1) (Eq. 3). The Day 1 data ($\hat{S}_{t=1,i}$) is estimated from the quadratic function derived from Eq. (2).

$$Normalized_Observation_t = \frac{S_{t,i}}{\hat{S}_{t=1,i}} \tag{3}$$

The last step is to combine the normalized observations of the three methods. As shown in Fig. 8, the standard deviations of the fitting residuals are different among the three methods, 0.75% for the DCC method, 0.78% for the ray-matching method and 1.54% for the desert method. Yet all the three methods result in very similar degradation fitting curves over the study period, especially the normalized DCC and ray-matching methods which are both based on bright clouds. The consistency in the trending distributions of the three methods indicates that the impact of wavelength dependent SRF degradation, if any, is very small and negligible on the radiometric degradation with these methods. A common fitting function thus should exist among the combined observations for the sensor degradation trending.

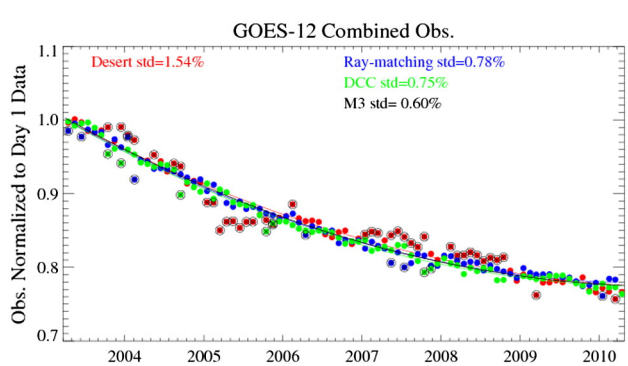

Fig. 8. Combined time-series of reference observations from different vicarious calibration methods after normalizations to the estimated data at the first day of operation. The crossed observations are the outliers identified with the recursive filtering method discussed in Section 3.2.

3.2. Integrated method to improve the relative calibration accuracy

3.2.1. Recursive filtering method

The recursive filtering method is employed to determine the common fitting function for the combined normalizations. It is assumed that residuals of the fitting function are of Gaussian distribution and any deviation of the fitting residual beyond a pre-defined threshold can be considered as an outlier (Wu, Sullivan, & Heidinger, 2010; Yu et al., 2014). This fitting and removal procedure is iteratively applied to the combined data until less than 3% of the observations are identified as outliers. The threshold in this study is defined as two-sigma value of the fitting residuals of each iterative loop.

The results of the recursive filtering at each loop applied to the combined three method data (M3) are shown in Fig. 9. Fig. 9a is the changes of outlier percentage, defined as the percentage of the outliers' number divided by the total number of observations at each loop, as well as the skewness and one standard deviation values of the fitting residuals. In this case, the outlier percentage drops below 3% at the fifth loop and becomes zero after the tenth loop as no more new outlier data is identified. The skewness is within ± 0.1 after the first recursive loop, indicating generally symmetric distribution of the fitting residual. As expected, the standard deviation of the fitting residuals progressively decreases with the continuous removal of outliers and becomes stable at 0.54% after the 10th loop. The distributions of the fitting functions of all the loops are very consistent (Fig. 9b), suggesting that the recursive filtering method can be used to generate a very robust sensor degradation trending.

As previously described, a threshold of 3% of the outlier percentage is used to break the recursive loop. A total of 53 observations out of 252 combined ones are identified as outliers after the fourth loop (Fig. 8). The majority of the outliers are from the desert data (38) with only seven from DCC and eight from ray-matching data. After the removal of the outliers, the standard deviation of the fitting residuals is reduced to 0.60%, less than that of any individual method. Sensitivity of the

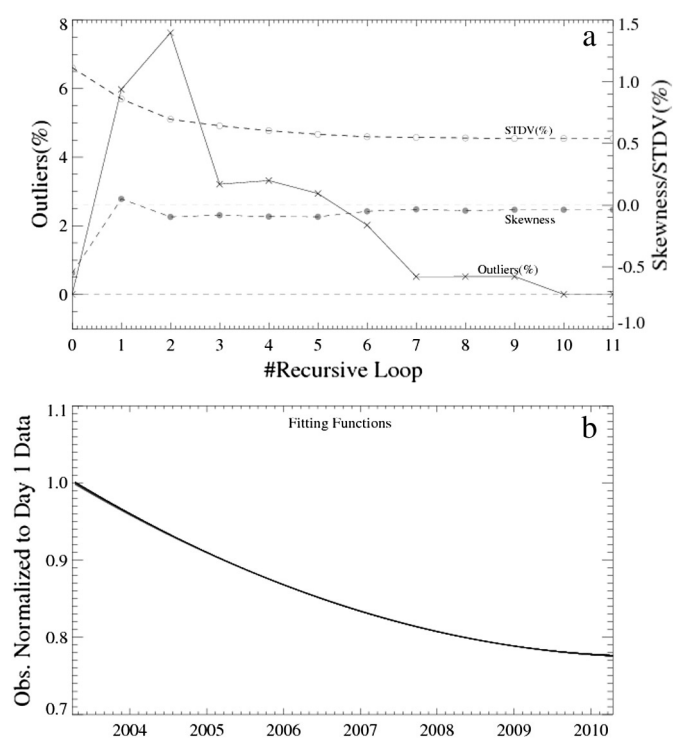

Fig 9. a: Outlier percentage and the skewness and the standard deviation values of the fitting residual at each loop; b: The 11 fitting functions of the 11 recursive loops in upper panel.

outliers to the pre-defined threshold is also tested with a set of different sigma values. The coefficients to multiple the sigma value range from one to three at interval of 0.5 (1.0, 1.5, 2.0, 2.5, and 3.0 times the sigma of fitting residuals). In this study, the outliers are the same with 53 outliers. This result may suggest that the trending function is not sensitive to the pre-defined threshold once the sigma coefficient is larger than a certain value.

3.2.2. Integrated method

The trending function derived after the recursive filtering over the combined three-method data (M3) is shown in Fig. 10, as well as the trending from each individual method. All these trending functions agree well with each other within less than 1% difference. The trending of the DCC method is the closest to the result of the integrated method within less than 0.1%. The desert has the largest trending difference from the integrated method at less than 1%, followed by the ray-matching method at less than 0.7%.

The impact of the desert data on the integrated method is examined by applying the integrated method on the combined DCC and ray-matching data only (M2). Similar to Figs. 8–10, Fig. 11 shows the results of recursive filtering at each loop (Fig. 11a and b) and trending results with the defined thresholds (Fig. 11c and d). As shown in Fig. 11a, the fitting residual is Gaussian-like distribution after the second loop and no new outlier can be identified since after the eighth loop. The derived fitting functions at each iterative loop are also very consistent as shown in Fig. 11b. With the thresholds applied in this study, the recursive filtering breaks at the fourth loop when the outlier percentage first drops to less than 3% (Fig. 11a), resulting in a total of 20 outliers out of 166 combined ones (10 outliers from each method). The standard deviation of the fitting residuals is reduced to 0.52% (Fig. 11c) and the trending function of the integrated method agrees well with that of DCC and ray-matching method. Similar to the result of M3 integrated method, the trending of the M2 integrated method is also much closer to that of DCC with difference less than 0.2% (Fig. 11d). That both M2 and M3 trending functions are close to DCC data may indicate that the trending result of the integrated method is not sensitive to the relatively large deviated distribution of one method data (e.g., the desert data in this study), although the removal of the desert data can result in reduced standard deviation values (0.60% for M3 vs. 0.52% for M2).

In summary, the integrated method described in this study includes the following steps: 1) Normalize the monthly observations of each method to their Day 1 data using the sensor degradation function. Seasonal variations in the monthly observations, if well characterized and understood, can be removed before normalization; 2) combine the normalized data of each method using the Day 1 data as the anchor date. Using Day 1 as the anchor time to combine the normalized data can help to distinguish the early deviation of the trending of each individual method, especially for the near real-time data analysis; and 3) use the recursive filtering method to select the observations from the combined data and derive the degradation trending function. Evaluation of each individual method can be applied before Step 3 by comparing the trending results of each method. This comparison can be conducted based on our current knowledge about the instrument performance and the characterization of the calibration reference (Fougnie, 2014). The knowledge-based removal of large noise method data can further reduce the trending uncertainty. In this study, since the Sonoran desert data is known for its relatively large short-term reflectance variation and the sensitivity to the climate variation events, it can be removed from the combined data for the recursive filtering and the standard deviation can be reduced from 0.60% at M3 data to 0.52% at M2 data.

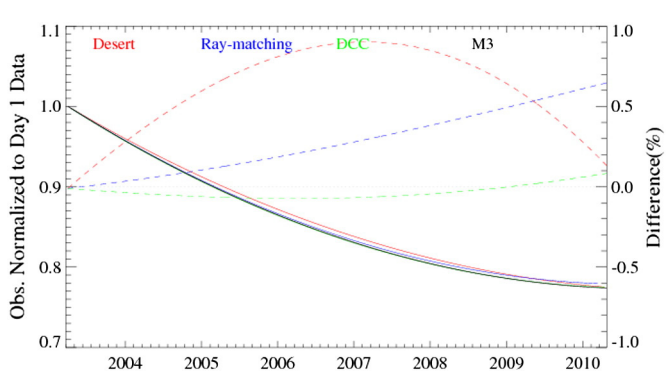

Fig. 10. Distributions of the fitting function over the combined data after recursive filtering (in black solid line), the desert data (in red solid line), the ray-matching data (in blue solid line), and the DCC data (in green solid line). The relative difference between the results of individual method to the combined one are also shown in dash lines which are referred to the second y-axis. (For interpretation of the references to color in this figure legend, the reader is referred to the web version of this article.)

3.3. Impacts on the near real-time calibration accuracy

Compared to the individual vicarious calibration method, the integrated method can result in reduced random error of the trending function. The reduced random error or relative calibration accuracy can provide better quality of calibrated radiance for the instruments without on-board calibration device. It can also be used to detect the calibration anomaly, if any, at a shorter period for the on-board calibration instruments (Bhatt et al., 2014). For these reasons, the application of the integrated method in the near real-time data analysis should be assessed.

The impacts of the integrated method to the near real-time data are examined with the GOES-12 data with M2 method in this study. Fig. 12a–c displays the time-series of the coefficients of the quadratic fitting function since after the fourth month of operation time. No fitting results are available for the first three months because at least four months of data are needed to generate the fitting quadratic function with uncertainty results. For each month since then on, the recursive filtering method is applied at every month over the combined data accumulated from the operation time through that month. Fig. 12d is the time-series of error budget calculated with the near real-time data. The random error (U_r) is calculated as the one standard deviation of the fitting residual after the recursive filtering. Using the trending of M2 integrated method over all the seven-year measurements as the reference, the systematic error (U_s) of each month is calculated as the relative difference between the near-real time trending and the reference one. The combined error (U_c) is the combination of random and systematic errors, calculated as $U_c = \sqrt{U_r^2 + U_s^2}$.

As shown in Fig. 12, quadratic and linear terms of the trending functions vary greatly in the about first and half years after the operation and both become stable since afterwards. The constant term of the fitting function also shows slightly larger variation in the about first two years, although its variation over whole mission period is very small within less than 0.5%. The systematic error does not become stable during the study period and displays the greatest variations in the first one year, ranging from almost 2% to less than −1%. This can be explained that that the fitting function is sensitive to the new measurements, especially when there are few data available in the early study period. The change of random error is relatively smooth. It increases dramatically in the first one year and becomes relatively stable after the first two years. As the results, the combined uncertainty is less than 2% in the first year and less than 1% afterwards. All these analyses indicate that about two years of measurements after operation should be needed to generate more robust calibration coefficients.

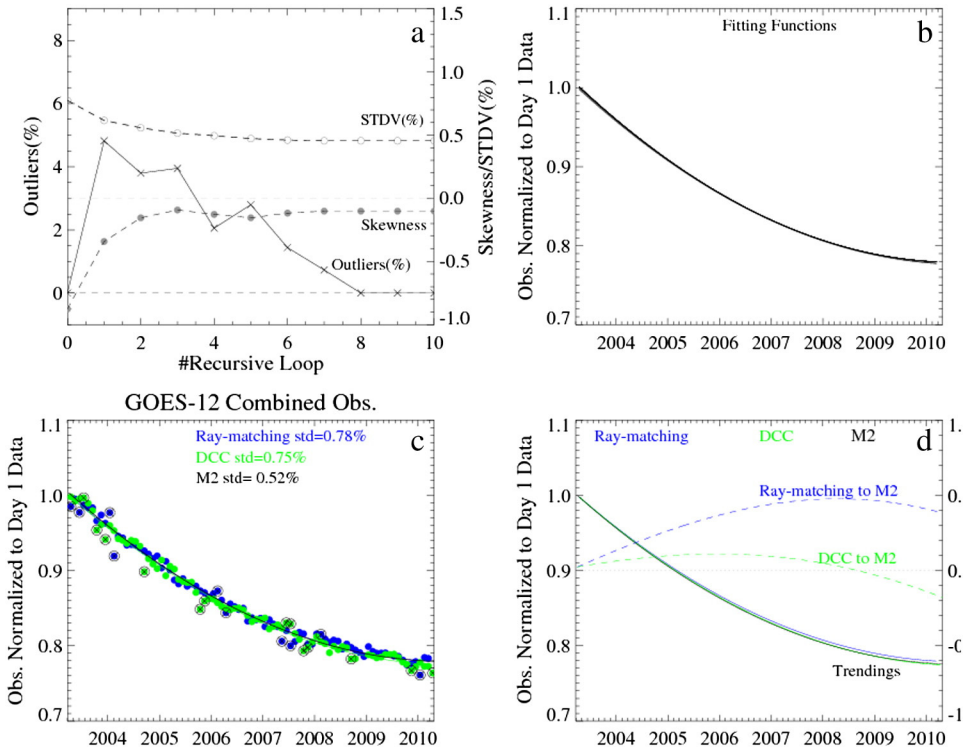

Fig. 11. Similar to Figs. 8–10, except that the input of the recursive filtering is the combined data from DCC and ray-matching (M2). Panel b consists of the 9 fitting functions of the 9 loops (#1 through #9) in Panel a.

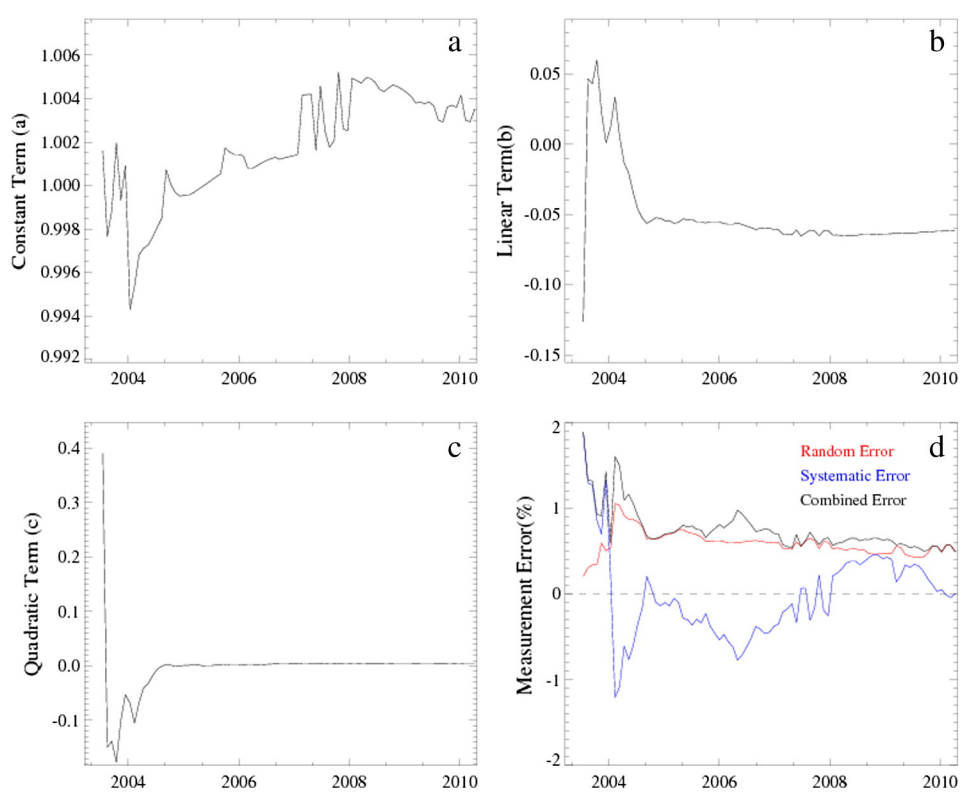

Fig. 12. Time-series of trending coefficients and the error budgets of integrated method for the 'near real-time' data. The coefficients are calculated with the fitting functions (Eq. 2) in which the unit of time t is year after operation. The time on x-axis starts with the GOES-12 operational date on April 1, 2003. No integrated method results are available in the first three months.

4. Transferring relative calibration to absolute calibration

Two steps are needed to convert the relative calibration results from the integrated method to the absolute ones traceable to Aqua MODIS. The first step is to reconstruct the pre-launch reflectance from the selected normalized observations with Eq. (4), and then generate the absolute calibration correction coefficients using the reflectance of the calibration reference targets with Eq. (5). The reflectance of the reference target is pre-defined and characterized with long-term Aqua MODIS C6 data.

$$R_{t,i} = \hat{R}_{t=1,i} \times Normalized_Observation_{t,int} \tag{4}$$

Where $\hat{R}_{t=1,i}$ is the estimated pre-launch reflectance of method i at the first day of operation ($t = 1$), calculated with the fitting quadratic function of vicarious calibration method (i) with Eq. (2); $Normalized_Observation_{t,int}$ is the normalized observations selected by the recursive filtering method from the combined data (integrated method) at time t calculated with Eq. (3).

$$Correction_Coefficient_{t,i} = \frac{\mathrm{Re}\,f_R_{t=1,i}}{R_{t,i}} * \frac{\hat{S}_{t=1,\mathrm{int}}}{\hat{S}_{t=1,i}} \tag{5}$$

where $\hat{S}_{i\,=\,1,\mathrm{int}}$ and $\hat{S}_{t\,=\,1,i}$ are the estimated observation at Day $t = 1$ from the quadratic functions of the integrated method and method i, respectively. $R_{t,i}$ is the re-constructed pre-launch calibration at time t for method i. $\mathrm{Re}f_R_{t\,=\,1,i}$ is the reflectance of reference target estimated with Aqua MODIS data for the method i at day $t = 1$.

The Day 1 DCC reference reflectance ($Ref_R_{t\,=\,1,i\,=\,dcc}$) is calculated with long-term mean MODIS reflectance of DCC (Eq. 6).

$$\mathrm{Re}f_R_{t=1,i=dcc} = \overline{R}_{\mathrm{modis},dcc} * SBAF_{dcc} \tag{6}$$

Where $\overline{R}_{\mathrm{modis},dcc}$ is the Aqua MODIS reference reflectance. $SBAF_{dcc}$ is the Spectral Band Adjustment Factor (SBAF) used to correct the GOES and MODIS spectral response function difference.

Due to the strong seasonal variation in the desert observations, Day 1 desert MODIS reflectance should be calculated with Eq. (7) for $t = 1$. About 12 years of clear-sky Aqua MODIS reflectance ($MODIS_R_{t,i\,=\,desert}$) are used to estimate the MODIS reflectance at GOES viewing geometric conditions (Yu et al., 2014).

$$\mathrm{Re}f_R_{t,i=desert} = \overline{R}_{\mathrm{modis},i=desert} \times SBAF_{desert} + m_1 \sin(\alpha t + \beta_1) + m_2 \sin(2\alpha t + \beta_2) \tag{7}$$

Where $\overline{R}_{\mathrm{modis},desert}$ (32.59%) is the long-term mean MODIS desert reflectance at GOES viewing geometries (Yu et al., 2014); m_1, m_2, α, β_1, and β_2 are the fitting coefficients for the seasonal variations of clear desert GOES-12 reflectance generated from Eq. (1).

The desert SBAF was calculated with Hyperion data (Yu et al., 2014) and the DCC SBAF was derived with SCIAMACHY data (Doelling et al., 2011). The corresponding parameters are given in Table 1.

The time-series of the calibration correction coefficients generated with DCC and desert reference reflectance are shown in Fig. 13. There is a small but significant difference (0.72%) between the DCC-based and Desert-based calibration coefficients ($p_value = 0.00$). The bias between these two absolute calibrations may come from uncertainties of the two Day 1 reference reflectance values. The uncertainty of Day 1 desert reference reflectance mainly comes from the function to correct the seasonality of desert reflectance and the BRDF model (Yu et al., 2014). In the future, long-term MODIS desert observations should be extended to ensure the reliability of desert reflectance on Day 1. The DCC reference reflectance in this study is determined with the ray-matching DCC observations which occur in a relatively smaller spatial domain, assuming that there is no spatial variation in the DCC reflectance over the GOES-12 DCC selection spatial domain. This assumption needs to be validated with the MODIS DCC reflectance across the whole GOES-12 DCC spatial domain in the future. Meanwhile, slight seasonal variations can be observed in the time-series of GOES-12 DCC reflectance (Fig. 6). As the result, there may exist a very slight difference between the long-term mean DCC reflectance and Day 1 value. In addition, recent research showed that GOES Imager scan mirror has slight angular dependent reflectivity (Yu et al., 2013). GOES-12 viewed the Sonoran desert at a fixed scan angle of about 2.5° from the nadir while the mean viewing angle of DCC pixels is at nadir with scan angle of 0°. This viewing angle difference may also attribute to the bias between the two sets of calibration coefficients.

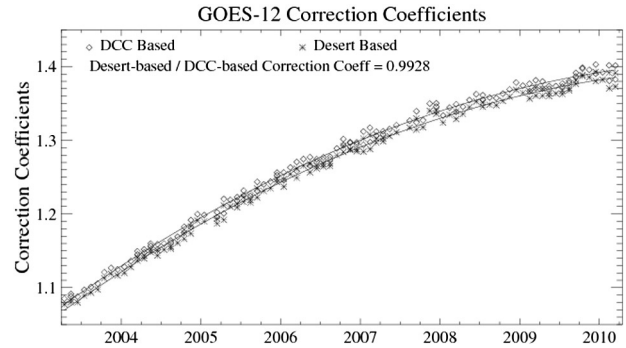

Fig. 13. Time-series of calibration correction coefficients tracing to Aqua MODIS C6 for the desert and DCC methods.

Table 1
Parameters used in Eqs. (5)–*(7).

Vicarious calibration method for G12	$\hat{R}_{t=1,i}$ (%)	$\overline{R}_{,\mathrm{modis},i}$ (%)	SBAF	$Ref_R_{t\,=\,1}$ (%)	$\hat{S}_{t\,=\,1,\mathrm{int}}/\hat{S}_{t\,=\,1,i}$
Desert	28.66	32.59	0.949[a]	31.10	1.00471
DCC	80.81	88.87	0.991[b]	87.98	1.00098

[a] Calculated with Hyperion data (Yu et al., 2014).
[b] Based on the GOES11 SRF using SCIAMACHY data (Doelling et al., 2011); GOES-11 and GOES-12 have almost identical Imager visible SRFs (Yu et al., 2014).

5. Conclusions

An integrated method is developed to combine results from multiple vicarious calibration methods, either relative or absolute calibration ones, to improve the relative calibration accuracy. Three vicarious calibration methods, DCC, desert and ray-matching methods, are applied to the GOES-12 Imager visible data as an example to describe this method. The time-series of monthly results from each method are first normalized to the values estimated on the first day of satellite operation. This normalization provides an anchor to link the results of relative calibrations to those of the absolute ones and thus allows for the absolute calibration traceable to a common reference. The normalized observations display very similar degradation pattern, indicating that the impact of the instrument wavelength dependent SRF degradation, if any, is very small or negligible on the radiometric calibration results with these vicarious calibration methods.

A recursive filtering method is applied to select the combined observations. Compared to the individual vicarious calibration method, the integrated method with the recursive filtering method to remove the outliers can improve the relative calibration accuracy and reduce the risk of the sensor degradation trending due to the long-term change of reference target and/or satellite measurements. As the result, for the instrument calibration with on-board calibration device such as GOES-R Advanced Baseline Imager (ABI), the integrated method can provide

an earlier calibration anomaly warning, if any. For the near real-time data analysis, it will take almost two years to derive the stable coefficients for the trending function.

Statistical analyses show that minimum thresholds of DCC and collocated high-reflectance cloud pixels are needed to generate reliable DCC reflectance and GEO–LEO reflectance ratio. Since clouds are more abundant over the GOES-East satellites' spatial domain than the GOES-West ones, it is expected that the calibration accuracy of the integrated methods for the GOES-West satellites may not be as good as for the GOES-East ones as described in this study. However, with the inputs of more observations resulted from other vicarious calibration methods (e.g., star and lunar calibration), the relative calibration accuracy of integrated cloud be further improved. It is expected that the integrated method will be a useful tool to validate the GOES-R ABI on-board radiometric calibration accuracy for the solar reflective channels.

The absolute calibration of the integrated method can be achieved with the generation of calibration correction coefficients using the reflectance of reference targets which are well characterized with the Aqua MODIS C6 data. There is less than 1.0% difference between the calibration correction coefficients derived with DCC and desert reference reflectance. Although the Sonoran desert is long-term stable at decade scale, the contribution of the desert observations to the trending function derived with the integrated method is very small. In fact, the trending functions derived with M2 and M3 integrated methods are both very close to that of DCC data at less than 0.2% and 0.1%, respectively. This may indicate that DCC may be more stable than the other method for the long-term trending. Yet, large abnormal reflectance was observed at some identified MODIS DCC pixels which marginally met the DCC temperature criteria. Since DCC is a selected common reference by the GSICS community, it is suggested that the microphysics of DCC should be further studied to provide the better understanding of the reference target.

Acknowledgments

We would like to thank Dr. Yong Chen for the LBLRTM simulation and Dr. Haifeng Qian for the valuable review comments. This work is partially funded by NOAA/NESDIS/STAR Calibration/Validation support. The constructive and valuable comments and suggestions from the three anonymous reviewers are much appreciated to improve the quality of this paper. The contents of this document are solely the opinions of the authors and do not constitute a statement of policy, decision, or position on behalf of NOAA or the U.S. government.

References

Angal, A., Chander, G., Xiong, X., Choi, T., & Wu, A. (2011). Characterization of the Sonoran Desert as a radiometric calibration target for Earth observing sensors. *Journal of Applied Remote Sensing*, *5* (059502-1-6).

Bhatt, R., Doelling, D., Wu, A., Xiong, X., Scarino, B., Haney, C., et al. (2014). Initial stability assessment of S-NPP VIIRS reflective solar band calibration using invariant desert and deep convective cloud targets. *Remote Sensing*, *6*, 2809–2826http://dx.doi.org/10.3390/rs6042809.

Bremer, J., Baucom, J., Vu, H., Weinreb, M., & Pinkine, N. (1998). Estimation of long-term throughput degradation of GOES 8 & 9 visible channels by statistical analysis of star measurements. *Proceedings of SPIE, Earth Observing Systems III*, *3439*, 145–154.

Chang, I. -L., Dean, C., Li, Z., Weinreb, M., Wu, X., & Swamy, P. (2012). Refined algorithms for star-based monitoring of GOES Imager visible channel responsivities. *SPIE*, *8510*, 85100R–85101Rhttp://dx.doi.org/10.1117/12.928892.

Chepfer, H., Minnis, P., Young, P., Nguyen, L., & Arduini, R. (2002). Estimation of cirrus cloud effective ice crystal shapes using visible reflectances from dual-satellite measurements. *Journal of Geophysical Research*, *107*(D23)http://dx.doi.org/10.1029/2000JD000240.

Clough, S., Shephard, M., Mlawer, E., Delamere, J., Iacono, M., Cady-Pereira, K., et al. (2005). Atmospheric radiative transfer modeling: A summer of the AER codes. *Journal of Quantitative Spectroscopy and Radiation Transfer*, *91*, 233–244.

Cosnefroy, H., Leroy, M., & Briottet, X. (1996). Selection and characterization of Saharan and Arabian desert sites for the calibration of optical satellite sensors. *Remote Sensing of Environment*, *58*, 101–114.

Doelling, D., Lukashin, C., Minnis, P., Scarino, B., & Morstad, D. (2012). Spectral reflectance corrections for satellite intercalibrations using SCIAMACHY data. *IEEE Geoscience and Remote Sensing Letters*, *1*, 119–123.

Doelling, D., Nguyen, L., & Minnis, P. (2004a). On the use of deep convective clouds to calibrate AVHRR data. *Proc. SPIE 49th Ann. Mtg, Earth Observing Systems IX conference, Denver, Colorado, August 2–6, 2004.*

Doelling, D., Minnis, P., & Nguyen, L. (2004b). *Calibration comparisons between SEVIRI, MODIS and GOES data, MSG RAO Workshop, Salzburg, Austria, Sept. 2004.*

Doelling, D., Morstad, D., Scarino, B., Bhatt, R., & Gopalan, A. (2013). The characterization of deep convective clouds as an invariant calibration target and as a visible calibration technique. *IEEE Transactions on Geoscience and Remote Sensing*, *51*(3), 1147–1159. http://dx.doi.org/10.1109/TGRS.2012.2225066.

Doelling, D., Morstd, D., Bhatt, R., & Scarino, B. (2011). Algorithm Theoretical Basis Document (ATBD) for Deep Convective Cloud (DCC). available at: https://gsics.nesdis.noaa.gov/pub/Development/AtbdCentral/GSICS_ATBD_DCC_NASA_2011_09.pdf

Ellord, G., & Bailey, A. (2007). Assessment of aircraft icing potential and maximum icing altitude from geostationary meteorological satellite data. *Weather and Forecasting*, *22*, 160–174http://dx.doi.org/10.1175/WAF984.1.

Eplee, R., Sun, J., Meister, G., Patt, F., Xiong, X., & McClain, C. (2011). Cross calibration of SeaWiFS and MODIS using on-orbit observations of the Moon. *Applied Optics*, *50*(2), 120–133.

Fougnie, B. (2014). *Combing VIS/NIR Methods, GSICS GRWG VIS/NIR Sub-group Webmeeting, 22 Oct. 2014.* (slides available online at https://gsics.nesdis.noaa.gov/wiki/Development/20141022).

Fougnie, B., Henry, P., Morel, A., Antoine, D., & Montagner, F. (2002). *Identification and characterization of stable homogeneous ocean zones: Climatology and impact on in-flight calibration of space sensor over Rayleigh scattering. Proc. of Ocean Optics XVI*, Santa Fe, New Mexico, 18–22 November, 2002.

Hagolle, O., Nicolas, J., Fougnie, B., Cabot, F., & Henry, P. (2002). Absolute calibration of VEGETATION derived from an interband method based on the Sun glint over ocean. *IEEE Transactions on Geoscience and Remote Sensing*, *42*, 1472–1481http://dx.doi.org/10.1109/TGRS.2004.826805.

Hayden, C., Wade, G., & Schmit, T. (1996). Derived product imagery from GOES-8. *Journal of Applied Meteorology*, *35*, 153–162.

Hu, Y., Wielicki, B., Yang, P., Stackhouse, P., Lin, B., & Young, D. (2004). Application of deep convective cloud albedo observation to satellite-based study of terrestrial atmosphere: Monitoring the stability of spaceborn measurement and assessing absorption anomaly. *IEEE Transactions on Geoscience and Remote Sensing*, *42*(11), 2594–2599.

Kieffer, H., & Stone, T. (2005). The spectral irradiance of the Moon. *Astronomy Journal*, *129*, 2887–2901.

Knapp, K. R. (2002). Quantification of aerosol signal in GOES 8 visible imagery over the United States. *Journal of Geophysical Research*, *107*(D20), 4426http://dx.doi.org/10.1029/2001JD002001.

Lacherade, S. (2013). Pleiades Orbital Lunar Observations (POLO) — Intensive study of the Moon. *GSICS Quarterly Newsletter*, *7*(3), 5.

Maturi, E., Harris, A., Merchant, C., Mittaz, J., Potash, B., Meng, W., et al. (2008). NOAA's sea surface temperature from operational geostationary satellites. *Bulletin of the American Meteorological Society*, *89*(12), 877–888http://dx.doi.org/10.1175/2008BAMS2528.

Pinker, R., Tarpley, J., Laszlo, I., Mitchell, K., Houser, P., Wood, E., et al. (2003). Surface radiation budgets in support of the GEWEX Continental-Scale International Project (GCIP) and the GEWEX Americas Prediction project (GAPP), including the North American Land Data Assimilation Systems (NLDAS) project. *Journal of Geophysical Research*, *108*(D22), 8844http://dx.doi.org/10.1029/2002JD003301.

Prins, E. M. (1996). News from fire research: The GOES-8 Automated Biomass Burning Algorithm (ABBA) introducing new capabilities for monitoring diurnal fire activity in the Western Hemisphere. *International Forest Fire News*, *49–52*.

Rao, C. R. N. (2001). Implementation of the post-launch vicarious calibration of the GOES imager visible channel. http://www.oso.noaa.gov/goes/goes-calibration/vicarious-calibration.htm

Romanov, P., Gutman, G., & Csiszar, I. (2000). Automated monitoring of snow cover over North America with multispectral satellite data. *Journal of Applied Meteorology*, *39*, 1866–1880.

Six, D., Fily, M., Alvain, S., Henry, P., & Benoist, J. -P. (2004). Surface characterization of the Dome Concordia area (Antarctica) as a potential satellite calibration site, using Spot 4/Vegetation instrument. *Remote Sensing of Environment*, *89*, 82–94.

Teillet, P., Barker, J., Markham, B., Irish, R., Fedosejes, G., & Storey, J. (2001). Radiometric cross-calibration of the Landsat-7 ETM + and Landsat-5 TM sensors based on tandem data sets. *Remote Sensing of Remote Sensing*, *78*, 39–54.

Wu, X., Menzel, W., & Wade, G. (1999). Estimation of sea surface temperature using GOES-8/9 radiance measurements. *Bulletin of the American Meteorological Society*, *80*, 1127–1138.

Wu, X., Qian, H., & Yu, F. (2011). Vicarious calibration of GOES visible channel using GOME-2. *Geoscience and Remote Sensing Symposium* (pp. 1033–1035)http://dx.doi.org/10.1109/IGARSS.2011. 6049310 (July 2011, Vancouver, Canada).

Wu, X., Stone, T., Yu, F., & Han, D. (2006). Vicarious calibration of GOES Imager visible channel using the Moon. *Conference on Characterization and Radiometric Calibration for Remote Sensing Proceedings of SPIE*, *6296*.

Wu, X., Sullivan, J., & Heidinger, A. (2010). Operational calibration of the Advanced Very High Resolution Radiometer (AVHRR) visible and near-infrared channels. *Canadian Journal of Remote Sensing*, *36*(5), 602–616.

Wu, X., & Sun, F. (2005). *Post-launch calibration of GOES Imager visible channel using MODIS. SPIE*, *5882*, http://dx.doi.org/10.1117/12.615401.

Yu, F., & Wu, X. (2013). Vicarious calibration of GOES Imager visible channels. *2013 EUMETSAT Satellite Conference and 19th AMS Satellite Conference, Vienna, Australia, 16–20 Sept.*

Yu, F., & Wu, X. (2014). NOAA operational implementation of DCC Correction. *2014 GSICS Annual Meeting, Darmstadt, Germany, March 10–14, 2014* (https://gsics.nesdis.noaa.gov/wiki/Development/20140324).

Yu, F., Wu, X., Grotenhuis, M., & Qian, H. (2014). Inter-calibration of GOES Imager visible channels over the Sonoran desert. *Journal of Geophysical Research-Atmosphere*, *119*, 8639–8659http://dx.doi.org/10.1002/2013JD020702.

Yu, F., Wu, X., Stone, T., & Sindic-Ranic, G. (2013). Angular variation of GOES Imager scan mirror visible reflectivity. *GSICS Quarterly Newsletter*, *7*(3), 9–10.

Zhang, X., Kondragunta, S., Ram, J., Schmidt, C., & Huang, H. (2012). Near real time global biomass burning emissions product from geostationary satellite constellation. *Journal of Geophysical Research*http://dx.doi.org/10.1029/2012JD017459.